Applied Physics Letters ARTICLE scitation.org/journal/apl

Improving near-room-temperature thermoelectrics in SnTe–MnTe alloys

Cite as: Appl. Phys. Lett. **116**, 193902 (2020); doi: 10.1063/5.0006739
Submitted: 5 March 2020 · Accepted: 22 April 2020 ·
Published Online: 12 May 2020

Zhiyu Chen,[1] Jing Tang,[2] Xuming Guo,[1] Fujie Zhang,[1] Mingjing Tang,[1] Fen Xiong,[3] Yue Chen,[3] and Ran Ang[1,4,a)]

AFFILIATIONS

[1]Key Laboratory of Radiation Physics and Technology, Ministry of Education, Institute of Nuclear Science and Technology, Sichuan University, Chengdu 610064, China
[2]Interdisciplinary Materials Research Center, School of Materials Science and Engineering, Tongji University, 4800 Caoan Road, Shanghai 201804, China
[3]Department of Mechanical Engineering, The University of Hong Kong, Pokfulam Road, Hong Kong, China
[4]Institute of New Energy and Low-Carbon Technology, Sichuan University, Chengdu 610065, China

[a)]Author to whom correspondence should be addressed: rang@scu.edu.cn

ABSTRACT

The rich capabilities for both electronic and phonon engineering in SnTe are highly desirable for achieving high thermoelectric performance. Alloying high-solubility MnTe (∼15%) leads to substitutional defects for reducing lattice thermal conductivity and band convergence for enhancing electronic performance, and thus, an improvement of thermoelectric performance of SnTe is realized. However, there is no evidence that the electronic and phonon transport properties are fully optimized in SnTe-15%MnTe thermoelectrics, especially for the near-room-temperature (< 573 K) thermoelectric performance, which still needs a sufficient promotion. Here, the substituted 2% Bi in SnTe-15%MnTe alloys dramatically increases the near-room-temperature zT and peak zT to ∼0.72 (at 550 K) and ∼1.3 (at 850 K), respectively. Combining the experimental evidence and the first-principles calculations, we demonstrate that the prominent enhancement of electronic performance arises from the Bi-doping-driven transport valence band alignment and the carrier concentration optimization. Furthermore, the Debye–Callaway model verifies that the reduction in lattice thermal conductivity is dominated by the Bi substitutional defects. The present findings reveal the importance of transport engineering in achieving high thermoelectric performance particularly near room temperature.

Thermoelectrics are of extensive interest for power generation due to the ability of direct energy conversion between heat and electricity.[1] These solid-state, emission-free energy materials have long been utilized for electrical power supply in deep-space missions and are promising for realizing a sustainable society by recovering the exhausted heat from vehicles and industries. However, the widespread utilization of thermoelectrics is limited by its relatively low conversion efficiency, which is determined by the dimensionless figure of merit $zT = S^2T/\rho(\kappa_e+\kappa_L)$, where S, T, ρ, κ_e, and κ_L are the Seebeck coefficient, the absolute temperature, the electrical resistivity, the electronic component of thermal conductivity, and lattice components of thermal conductivity, respectively.[2]

Numerous efforts have been dedicated to improving the figure of merit zT. In addition to the carrier concentration optimization for balancing the interdependent parameters S, ρ, and κ_e,[3] the band structure and microstructure engineering have been demonstrated to be the design routes to realize excellent thermoelectric performance, including band convergence,[4] resonant doping,[5] point defects,[6] and dislocations.[7] Such approaches are extremely successful in SnTe thermoelectrics, which are characterized by the rock-salt structure and two-valence band structure. Particularly, alloying SnTe with monotelluride such as HgTe,[8] CdTe,[9–12] CaTe,[13,14] MgTe,[15,16] and MnTe[17–21] can trigger a remarkable increase in valley degeneracy N_v. As a typical representative, MnTe has been verified to be one of the most effective compounds for minimizing the energy offset $\Delta E_{L\text{-}\Sigma}$ between the L band and the Σ band owing to its relatively high solubility (∼15%) in SnTe. Unfortunately, there still remains a residual energy offset for completely aligning the transporting valence bands due to the limited solubility of MnTe. Recently, the solubility of MnTe has further increased to ∼20% in SnTe with the help of 5% GeTe, enabling a full optimization of the valence band structure.[19] However, both GeTe and the increased MnTe concentration alloyed in SnTe induce a significant deviation in the carrier concentration from its optimum, leading to a considerable challenge for zT enhancements.[18,19] In addition, the relative lower near-room-temperature zT intrinsically limits the advance of average zT_{avg} and thus the practical applications of various

SnTe–MnTe alloys. Therefore, seeking another effective strategy for improving thermoelectric performance in SnTe-15%MnTe alloys is highly desirable.

This motivates the current work focused on the transport properties of Bi-substituted SnTe–MnTe alloys. The exotic Bi substitution enables both an optimization of the carrier concentration and maximal transport valence bands for enhancing the electronic performance in SnTe. The Bi substitution also enables an effective stress and mass fluctuation for strengthening the phonon scattering, leading to an apparent reduction in lattice thermal conductivity κ_L. Ultimately, a peak zT of ~1.3 at 850 K is achieved in SnTe-15%MnTe-2%Bi without relying on other approaches for phonon scattering, which can be comparable to many superior SnTe-based thermoelectric materials.[9,16,17,19,22–24] Moreover, the 2% Bi substituted sample shows an enhanced near-room-temperature zT compared to different SnTe-based thermoelectrics, further demonstrating the significance of Bi in synergistically manipulating transport properties for promoting the improvement of thermoelectric performance in SnTe alloys.

The room temperature x-ray diffraction (XRD) patterns for $Sn_{0.87-x}Mn_{0.15}Bi_xTe$ ($x = 0$ – 0.05) samples are shown in Fig. 1(a). All the main diffraction peaks correspond well to the NaCl-type cubic structure of SnTe. For the sample with $x \leq 0.02$, no impurity phase is observed within the detection limit. Once the Bi content is higher than 3%, the impurity of Bi (~27.3°) is observed, while the substituted content is lower than the solubility limit. The results of structural Rietveld refinement show that the lattice parameter a gradually increases with the increasing Bi content owing to the larger ionic radius of Bi than that of Sn [see Fig. 1(b) and Fig. S1 in the supplementary material]. When $x \geq 0.03$, the lattice expansion can be negligible due to the emergence of the Bi-rich phase, demonstrating that the solubility of Bi is less than 0.03. Additionally, the room-temperature carrier concentration n_H gradually decreases for $x < 0.03$, confirming the substitution of the Sn sublattice by Bi [see Fig. 1(b)]. As for the sample with $x = 0.05$, the reduced carrier concentration may be due to the formation of Bi and Mn impurity phases.

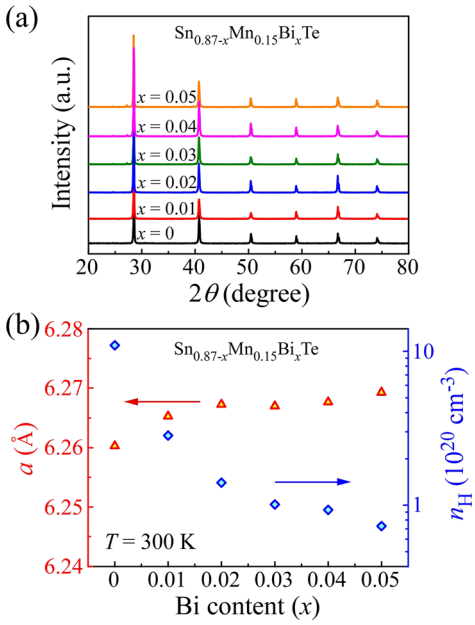

FIG. 1. (a) Room temperature powder x-ray diffraction (XRD) patterns and (b) lattice parameter a and carrier concentration n_H at room temperature for the $Sn_{0.87-x}Mn_{0.15}Bi_xTe$ samples ($x = 0$–0.05).

Much direct evidence for the element distribution derives from scanning electron microscopy (SEM) and energy-dispersive spectroscopy (EDS). No second phase is observed for the sample with $x = 0$ [see Fig. 2(a)]. However, trace impurities with various sizes embedded in the matrix are detected for the sample with $x = 0.05$, which is indexed as the Bi and Mn precipitates [see Fig. 2(b) and Fig. S2 in the supplementary material], revealing that the solubility of Bi and Mn can be affected by each other.

The electrical properties including resistivity ρ and Seebeck coefficient S for $Sn_{0.87-x}Mn_{0.15}Bi_xTe$ are shown in Fig. 3. Both the resistivity and the Seebeck coefficient enhance with the increasing Bi content at relatively low temperature. Particularly, the Seebeck coefficient for $x = 0.05$ (~113 μV K^{-1}) is twice higher than that for $x = 0.01$ (~60 μV K^{-1}) at room temperature. While at temperatures above 750 K, the degenerated electrical properties can be attributed to the bipolar diffusion for the samples with a higher Bi content, a similar variation can be found in other Bi-doped SnTe alloys.[24]

To reveal the origin of the increased electronic performance for the Bi-substituted SnTe-15%MnTe alloys, the carrier concentration-dependent Seebeck coefficient S, Hall mobility μ_H, and power factor PF at room temperature are shown in Fig. 4. The gray curves are the plots calculated on the basis of the two-band model, which has shown its validity for predicting the electronic properties of SnTe.[18,19,25] Evidently, the electronic properties of all the doped materials show a noticeable deviation from the model prediction. Specifically, the Seebeck coefficient of the sample with $x = 0.01$ is slightly higher than that of SnTe-15%MnTe alloys (dashed black curves, see Fig. S3 in the supplementary material). With the increasing Bi content, the Seebeck coefficient is further enhanced and can be comparable to that of SnTe-5%GeTe-20%MnTe at the given carrier concentration (see Fig. S3 in

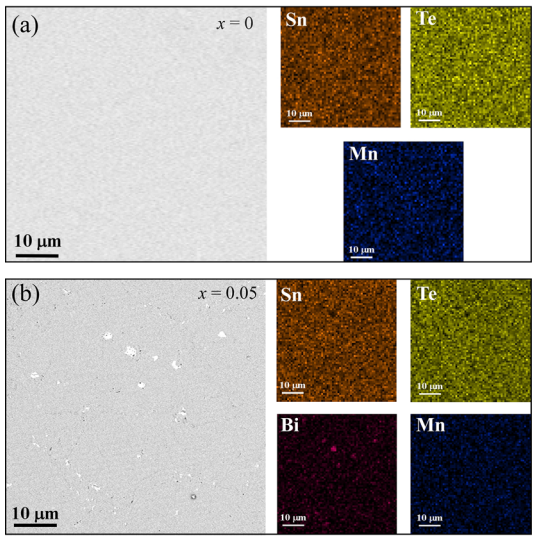

FIG. 2. Scanning electron microscopy (SEM) and corresponding energy-dispersive spectroscopy (EDS) mapping for (a) $Sn_{0.87}Mn_{0.15}Te$ and (b) $Sn_{0.82}Mn_{0.15}Bi_{0.05}Te$.

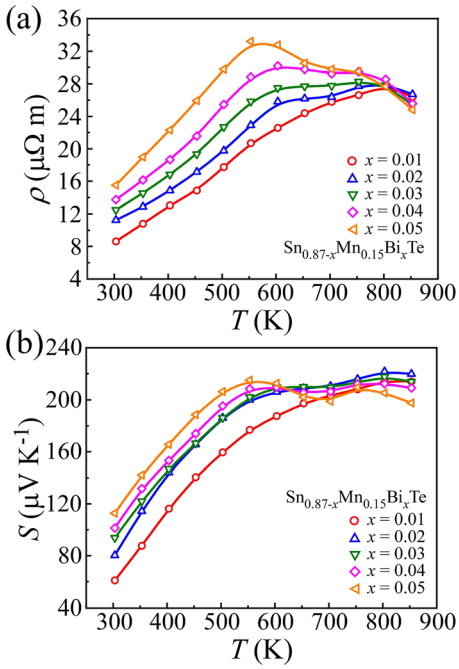

FIG. 3. Temperature-dependent (a) resistivity ρ and (b) Seebeck coefficient S for $Sn_{0.87-x}Mn_{0.15}Bi_xTe$.

the supplementary material).[19] Such a result provides a good clarification on the Bi substitution aligning the valence bands in SnTe.

This is further rationalized through first-principles calculations in which three different generalized quasi random structures with the lowest structural order are considered for $Sn_{23}Mn_4Te_{27}$ and $Sn_{22}Mn_4BiTe_{27}$. Clearly, the bandgap is reduced due to Bi doping in SnTe–MnTe alloys, which is responsible for the bipolar diffusion in the sample with a higher Bi content. It is also seen that $Sn_{22}Mn_4BiTe_{27}$ generally has a larger density of state near the valence band maximum (see Fig. 5), triggering an enhanced density of state mass m^* for the Bi substituted samples at a given carrier concentration (see Fig. S4 in the supplementary material). As is well known, the density of state mass is defined by $m^* = N_V^{2/3} m_b^*$, where N_v and m_b^* are the number of equivalent degenerated valleys and the band effective mass, respectively.[26] Namely, both the higher N_v and m_b^* result in the improved density of state mass. However, the large m^* caused by improving m_b^* (i.e., by flattening the band) can lead to a considerable reduction in mobility and thus decrease the electronic performance despite the resulting increased Seebeck coefficient. In fact, either the higher power factor or the undeteriorated mobility (compared to that of SnTe-15%MnTe with lower alloying defects) demonstrates that the enhanced m^* is mainly attributed to the more converged valence bands.

In addition to the discussion on the electronic structure calculations and effective mass, the temperature dependent Hall coefficient R_H is another persuasive experimental evidence for the ideal valence band convergence for the current Bi-substituted SnTe–MnTe alloys. Due to the two-band-transport of charge carriers in SnTe, the peak of R_H appears when the L band and the Σ band with different mobilities contribute identical conduction, which is considered as a good indication of band convergence.[18,27,28] This implies that a smaller energy

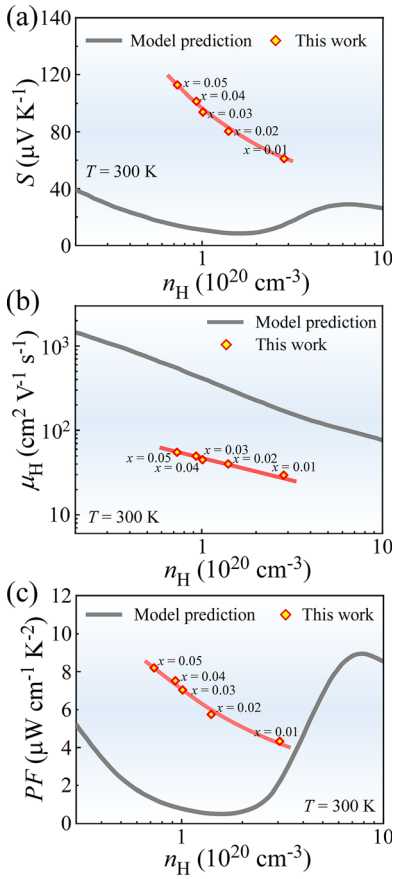

FIG. 4. (a) Carrier concentration-dependent Seebeck coefficient S, (b) Hall mobility μ_H, and (c) power factor at 300 K for $Sn_{0.87-x}Mn_{0.15}Bi_xTe$, with a comparison to theoretical predication (gray curves).

offset $\Delta E_{L\text{-}\Sigma}$ can lead to a lower temperature of the R_H peak. Obviously, the sample with $x = 0.01$ shows a decrease in the peak temperature compared to SnTe-15%MnTe (~650 K).[18] However, no R_H peak is observed at $T < 600$ K for the samples with $x \geq 0.02$, indicating that the valence bands act as a single band transport by the additional Bi substitution [see Fig. 6(a)].[14,19]

Temperature-dependent Hall mobility μ_H is shown in Fig. 6(b). Evidently, the mobility is significantly reduced owing to the increased carrier concentration, band convergence, and defect scattering in comparison with pristine SnTe. Largely benefiting from the reduced carrier

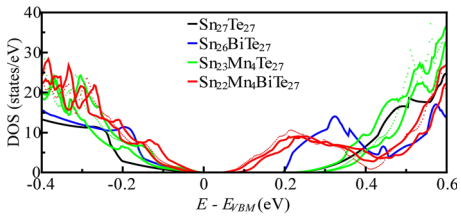

FIG. 5. Electronic density of states (DOS) of pristine SnTe and different SnTe alloys. The valence band maximum (VBM) is shifted to 0 eV.

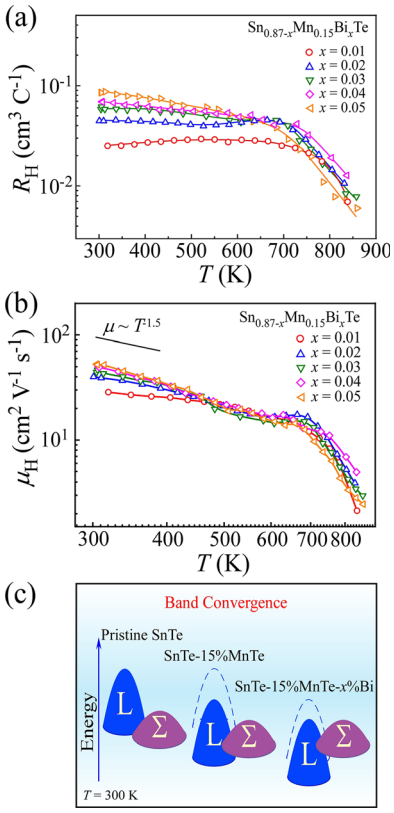

FIG. 6. Temperature-dependent (a) Hall coefficient R_H and (b) Hall mobility μ_H for $Sn_{0.87-x}Mn_{0.15}Bi_xTe$. (c) Schematic diagram of the band structure on the evolution of SnTe with doping Mn and Bi.

concentration, the mobility for the samples in this work increases with the increasing Bi content. Moreover, the Hall mobility for $Sn_{0.87-x}Mn_{0.15}Bi_xTe$ decreases with elevating temperature roughly via $\mu_H \sim T^{-1.5}$, indicating the unchanged acoustic phonon scattering mechanism.[29] Figure 6(c) shows the schematic diagram of the band structure on the evolution of SnTe. Due to the co-doping of Bi and Mn, the valence bands in SnTe are well aligned, while with the increasing temperature, the L band moves downward, leading to a less-converged valence bands and the resulting reduction in the Seebeck coefficient at ~550 K [see Fig. 3(b)].[19]

Alloying SnTe–MnTe with Bi not only enables well-aligned valence bands for optimizing electronic performance but also induces effective phonon scattering to decrease the lattice thermal conductivity. The total thermal conductivity κ is calculated by $\kappa = dC_pD$ (D is the thermal diffusivity; see Fig. S5 in the supplementary material). The lattice thermal conductivity κ_L is obtained via the Wiedemann–Franz law ($\kappa_e = LT/\rho$) from κ, where L is the Lorenz number [see Fig. 7(a)]. κ and κ_L as a function of temperature are shown in Fig. 7(b). Exactly, κ_L decreases with the increasing Bi content below 600 K, indicating the enhanced phonon scattering. It might be noted that at elevated temperature, κ_L enhances with the increasing Bi content. Such a variation is similar to that of the Seebeck coefficient.

Understanding the inherent relationship between the lattice thermal conductivity reduction and phonon-scattering origin is of significance to designing high-efficient thermoelectrics. Lattice softening and

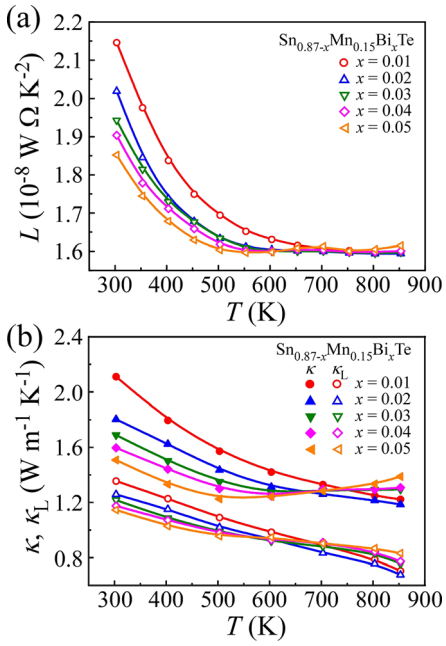

FIG. 7. Temperature-dependent (a) Lorenz number and (b) total thermal conductivity κ and lattice thermal conductivity κ_L.

phonon anharmonicity play a positive role in reducing κ_L.[30–32] However, the almost constant sound velocities and Grüneisen parameter with the increasing Bi content at room temperature reveal the negligible effects of lattice softening and phonon anharmonicity [see Fig. 8(a)]. The Debye–Callaway model is utilized to confirm the effect on the reduction in lattice thermal conductivity by only considering the Umklapp phonon scattering and point defects (see the details in the supporting material).[33] Obviously, for the samples with $x \leq 0.02$, the κ_L values are in agreement with the predicted values [see Fig. 8(b)], indicating that the Bi substitutional defects dominate the transport mechanism. However, the other samples show an evident deviation from the above prediction curve. This is because the model utilized here overestimates the contribution of point defects that originate from the formation of precipitates, while the relatively large-size precipitates here are unlikely to significantly affect the phonon scattering.

The temperature-dependent thermoelectric figure of merit zT is shown in Fig. 8(c). The synergistic optimization of thermoelectric properties enables a significant improvement of zT upon Bi and Mn substitution. Eventually, a maximum zT of ~1.3 is obtained for $x = 0.02$ at 850 K. It should be noted that only relying on substitutional defects for reducing lattice thermal conductivity, the realized high zT in this work can be comparable to various SnTe-based alloys with excellent thermoelectric performance (see Fig. S6 in the supplementary material).[9,16,17,19,22–24] More importantly, the improvement of the near-room-temperature zT (up to ~0.72 at 550 K) advances the average ZT_{avg} of current 2%, where the Bi-substituted SnTe–MnTe alloy outperforms other SnTe–MnTe thermoelectric materials, indicating the superior application potential (see Fig. S6 in the supplementary material).[17–21] In addition, the high zT is also found to be highly reproducible and repeatable (see Figs. S7 and S8 in the supplementary material).

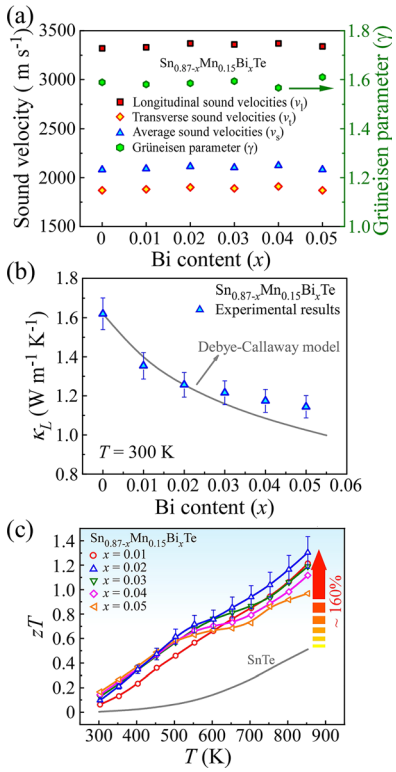

FIG. 8. (a) Room temperature longitudinal (v_l), transverse (v_t), and average (v_s) sound velocities and Grüneisen parameter γ. (b) lattice thermal conductivity κ_L for $Sn_{0.87-x}Mn_{0.15}Bi_xTe$. The gray solid curve represents the fitted results of the Debye–Callaway model. (c) Temperature-dependent figure of merit zT for $Sn_{0.87-x}Mn_{0.15}Bi_xTe$, with a comparison to pristine SnTe.

In conclusion, this work demonstrates the significance of Bi for systematically manipulating the electronic and phonon transport properties of SnTe–MnTe thermoelectric materials. Such a Bi substitution enables both an optimization of the carrier concentration and aligned transporting valence bands for enhancing the electronic performance. Simultaneously, the Bi substitution strengthens the phonon scattering for a reduction in lattice thermal conductivity. The synergistic effects enabled by Bi substitution lead to a remarkable improvement of both near-room-temperature zT and peak zT achieved for $x = 0.02$. The present findings confirm the validity of Bi substitution for increasing zT of SnTe thermoelectric materials in the whole temperature range via optimizing thermoelectric transport properties.

See the supplementary material for the experimental details, computational details, temperature dependence of current zT in comparison with previous results, etc.

This work was financially supported by the National Key Research and Development Program of China (Grant No. 2018YFA0702100), the Joint Funds of the National Natural Science Foundation (NNSF) of China and the Chinese Academy of Sciences' Large-Scale Scientific Facility (Grant No. U1932106), the NNSF of China (Grant No. 51771126), the Youth Foundation of Science & Technology [Department of Sichuan Province in China (Grant No. 2016JQ0051)], the Thousand Talents Program of Sichuan Province in China, and the World First-Class University Construction Funding of China. F. Xiong and Y. Chen are grateful for the financial support from RGC under Project Nos. 17200017 and 17300018 and the research computing facilities offered by ITS, HKU. The authors thank Professor Yanzhong Pei from Tongji University for his support and discussion on the Hall measurement. Z. Y. Chen and J. Tang contributed equally to this work.

The data that support the findings of this study are available within this article.

REFERENCES

[1]L. E. Bell, Science **321**, 1457 (2008).
[2]G. J. Snyder and E. S. Toberer, Nat. Mater. **7**, 105 (2008).
[3]Q. Zhang *et al.*, Adv. Energy Mater. **5**, 1401977 (2015).
[4]Y. Pei *et al.*, Nature **473**, 66 (2011).
[5]J. P. Heremans *et al.*, Science **321**, 554 (2008).
[6]M. Hong *et al.*, J. Am. Chem. Soc. **141**, 1742 (2019).
[7]Z. Chen *et al.*, Nat. Commun. **8**, 13828 (2017).
[8]G. Tan *et al.*, Energy Environ. Sci. **8**, 267 (2015).
[9]G. Tan *et al.*, J. Am. Chem. Soc. **136**, 7006 (2014).
[10]L. J. Zhang *et al.*, J. Mater. Chem. A **6**, 2507 (2018).
[11]J. Tang *et al.*, ACS Energy Lett. **3**, 1969 (2018).
[12]J. He *et al.*, RSC Adv. **6**, 32189 (2016).
[13]R. Al Rahal Al Orabi *et al.*, Chem. Mater. **28**, 376 (2016).
[14]Z. Chen *et al.*, Appl. Phys. Lett. **115**, 073903 (2019).
[15]A. Banik *et al.*, Chem. Mater. **27**, 581 (2015).
[16]J. Tang *et al.*, Mater. Today Phys. **9**, 100091 (2019).
[17]W. Li *et al.*, Adv. Mater. **29**, 1605887 (2017).
[18]W. Li *et al.*, J. Materiomics **1**, 307 (2015).
[19]J. Tang *et al.*, Adv. Funct. Mater. **28**, 1803586 (2018).
[20]H. Wu *et al.*, Energy Environ. Sci. **8**, 3298 (2015).
[21]G. Tan *et al.*, J. Am. Chem. Soc. **137**, 11507 (2015).
[22]J. Hwang *et al.*, ACS Nano **13**, 8347 (2019).
[23]S. Roychowdhury *et al.*, ACS Energy Lett. **4**, 1658 (2019).
[24]H. Tan *et al.*, ACS Appl. Mater. Interfaces **11**, 23337 (2019).
[25]M. Zhou *et al.*, Phys. Chem. Chem. Phys. **16**, 20741 (2014).
[26]H. J. Goldsmid, *Thermoelectric Refrigeration* (Plenum Press, NewYork, 1964).
[27]I. A. Chernik *et al.*, Sov. Phys. Semicond. **2**, 645 (1968).
[28]H. Sun *et al.*, Phys. Chem. Chem. Phys. **16**, 15570 (2014).
[29]Y. I. Ravich, B. A. Efmova, and I. A. Smirnov, *Semiconducting Lead Chalcogenides* (Plenum Press, New York, 1970).
[30]Z. Chen, X. Zhang, and Y. Pei, Adv. Mater. **30**, 1705617 (2018).
[31]Y. Tian *et al.*, Phys. Rev. B **95**, 094104 (2017).
[32]D. Das *et al.*, Phys. Rev. B **96**, 064116 (2017).
[33]B. Abeles, Phys. Rev **131**, 1906 (1963).